# Does the Madden–Julian Oscillation Influence Wintertime Atmospheric Rivers and Snowpack in the Sierra Nevada?

BIN GUAN AND DUANE E. WALISER

*Jet Propulsion Laboratory, California Institute of Technology, Pasadena, California*

NOAH P. MOLOTCH

*Department of Geography and Institute for Arctic and Alpine Research, University of Colorado, Boulder, Colorado, and Jet Propulsion Laboratory, California Institute of Technology, Pasadena, California*

ERIC J. FETZER

*Jet Propulsion Laboratory, California Institute of Technology, Pasadena, California*

PAUL J. NEIMAN

*Physical Sciences Division, NOAA/Earth System Research Laboratory, Boulder, Colorado*

(Manuscript received 8 April 2011, in final form 2 August 2011)

ABSTRACT

The relationships between the Madden–Julian oscillation (MJO), activities of atmospheric rivers (ARs), and the resulting snowpack accumulation in the California Sierra Nevada, are analyzed based on 13 yr of observations for water years 1998–2010 inclusive. The AR activity, as measured by the number of high-impact ARs, mean per event snow water equivalent (SWE) changes, and the cumulative SWE changes, is shown to be significantly augmented when MJO convection is active over the far western tropical Pacific (phase 6 on the Wheeler–Hendon diagram). The timing of high-impact ARs (early- versus late-winter occurrences) also appears to be regulated by the MJO.

Total snow accumulation in the Sierra Nevada (i.e., AR and non-AR accumulation combined) is most significantly increased when MJO convection is active over the eastern Indian Ocean (phase 3), and reduced when MJO convection is active over the Western Hemisphere (phase 8), with the magnitude of the daily anomaly being roughly half the cold-season mean daily snow accumulation over many snow sensor sites. The positive (negative) SWE anomaly is accompanied by a cold (warm) surface air temperature (SAT) anomaly and an onshore (offshore) water vapor flux anomaly. The contrasting SAT anomaly patterns associated with MJO phases 3 and 8, revealed by the in situ observations, are more realistically represented in the Atmospheric Infrared Sounder retrievals than in the European Centre for Medium-Range Weather Forecasts Interim reanalysis.

## 1. Introduction

Much of the wintertime precipitation in California and other West Coast states is fueled by the influx of moisture carried by extratropical cyclones, which is favored/enhanced by the regional topography as the moist air is blocked and lifted upward along the mountain slopes (e.g., Alpert 1986; Pandey et al. 1999; Hayes et al. 2002; Neiman et al. 2002, 2009). Various studies have established the connections between precipitation amount and the strength of the upslope airflow/water vapor flux during orographic precipitation events (Pandey et al. 1999; Neiman et al. 2002, 2009). Atmospheric rivers (ARs), in particular, are found to be a leading contributor to extreme precipitation and hydrological events in the West Coast states (Ralph et al. 2006; Neiman et al. 2008a,b; Leung and Qian 2009; Dettinger et al. 2011). Characterized by enhanced water vapor flux in long, narrow channels, ARs are responsible for transporting the majority of

*Corresponding author address:* Bin Guan, Jet Propulsion Laboratory, California Institute of Technology, M/S 233-300, 4800 Oak Grove Dr., Pasadena, CA 91109.
E-mail: bin.guan@jpl.nasa.gov

DOI: 10.1175/MWR-D-11-00087.1

the meridional water vapor flux over the globe (Zhu and Newell 1994, 1998). Orographic precipitation is favored when strong water vapor flux is directed toward mountainous terrain. In California, ~30%–40% of the total seasonal snow accumulation is contributed by landfalling ARs in most years, with the AR contribution dominated by just 1–2 extreme events in some years (Guan et al. 2010).

Early prediction of winter storm activities is critical to water resource management in the semiarid western states, where snowmelt from the seasonal snowpack forms an important water supply during the dry season (Bales et al. 2006). In this regard, the mountain snowpack in the Sierra Nevada provides approximately 75% of the water supply for California's central valley agricultural sector. An improved understanding of the coupled atmosphere–ocean–land surface processes, which control the timing and magnitude of snow accumulation, is critical for subseasonal (and longer) scale projections of water availability and demand. In particular, ARs concern weather forecasters and emergency managers as they are both a natural water resource and a potential flood-producing hazard. Non-AR storms, which contribute ~60%–70% of the total seasonal snow accumulation in most years, are also of concern from water resource and management perspectives. Although the skill of quantitative precipitation forecasts is fairly low in this region (Grubišić et al. 2005), weekly to subseasonal prediction of precipitation and related snowpack status may be possible if storm activities are considerably mediated by the slowly varying large-scale atmospheric/oceanic conditions, such as those related to the Madden–Julian oscillation (MJO).

It is generally understood that the tropical/subtropical Pacific Ocean has far reaching impacts on the U.S. weather and climate. A number of studies have linked the MJO to changes in the North Pacific circulation patterns and West Coast precipitation (Higgins and Mo 1997; Mo and Higgins 1998; Bond and Vecchi 2003; Jones 2000; Jones et al. 2004). Mo and Higgins (1998) found winter precipitation in California is favored by enhanced convection in the equatorial Pacific near 150°E relatable to MJO. Jones (2000) found that California tends to receive slightly more precipitation extremes when MJOs are active in the Indian Ocean. The concept of ARs provides a new, unique perspective to investigate the tropical/subtropical impact on the extratropics. The ARs, which critically rely upon extratropical cyclogenesis and moisture supply from the tropics/subtropics (Zhu and Newell 1994), are likely to be affected by the MJO, El Niño–Southern Oscillation (ENSO), and other low-frequency modes through changes in the mean atmospheric circulation, such as the location and strength of the waveguiding Pacific jet (Mo and Higgins 1998). A recent case study by Ralph et al. (2011) illustrated the role of MJO convection in the eastern Indian Ocean in setting up the large-scale circulation background favorable for the development of a strong AR that made landfall in the Pacific Northwest in March 2005. A comprehensive understanding of the tropical impacts on AR activity awaits continued observation and analysis efforts.

Recognizing the unique role of ARs in regional weather, hydrology, and water resources, and the current lack of understanding on AR's tropical forcing/connections and extended-range (one week and beyond) predictability, the current study explores the largely unknown climatological relationship between MJO and ARs based on the analysis of a relatively long period of in situ and satellite data. The importance of non-AR storms, as noted earlier, is also factored in. Focusing on snow accumulation in California's Sierra Nevada, the study clarifies the MJO influence on the intensity and timing of landfalling ARs, as well as the MJO modulation of the total seasonal snow accumulation, which integrates the effects from both AR and non-AR storms. Data and methods are described in section 2. Section 3 discusses the intensity of Sierra Nevada snowfall and the contribution of ARs to extreme events. The influence of MJO on AR and the seasonal snowpack is detailed in sections 4–6. Conclusions are given in section 7.

## 2. Data and methods

### *a. Snow water equivalent*

Winter precipitation is relatively difficult to measure in complex mountainous terrain given poor gauge catch efficiencies for snowfall. Precipitation for a given storm event can be well proxied by changes in the snow water equivalent (SWE), for which measurements are more accurately made using a snow pillow. In situ SWE observations are obtained from 100 snow sensor sites (Fig. 1a, dots) in the Sierra Nevada operated by the California Department of Water Resources. Each site consists of a snow pillow, and precipitation and temperature gauges (temperature data are described in more detail below). All sites used in this analysis are above 1500-m elevation. Daily SWE values are available for these sites dating back to the late 1970s although the main analysis period for this study is water year[1] (WY) 1998–2010. For comparison, we also use gridded SWE data from the high-resolution (1 km × 1 km) Snow Data Assimilation System (SNODAS), developed by the National Operational

[1] A water year is a 12-month period between 1 October and 30 September, and designated by the calendar year in which it ends.

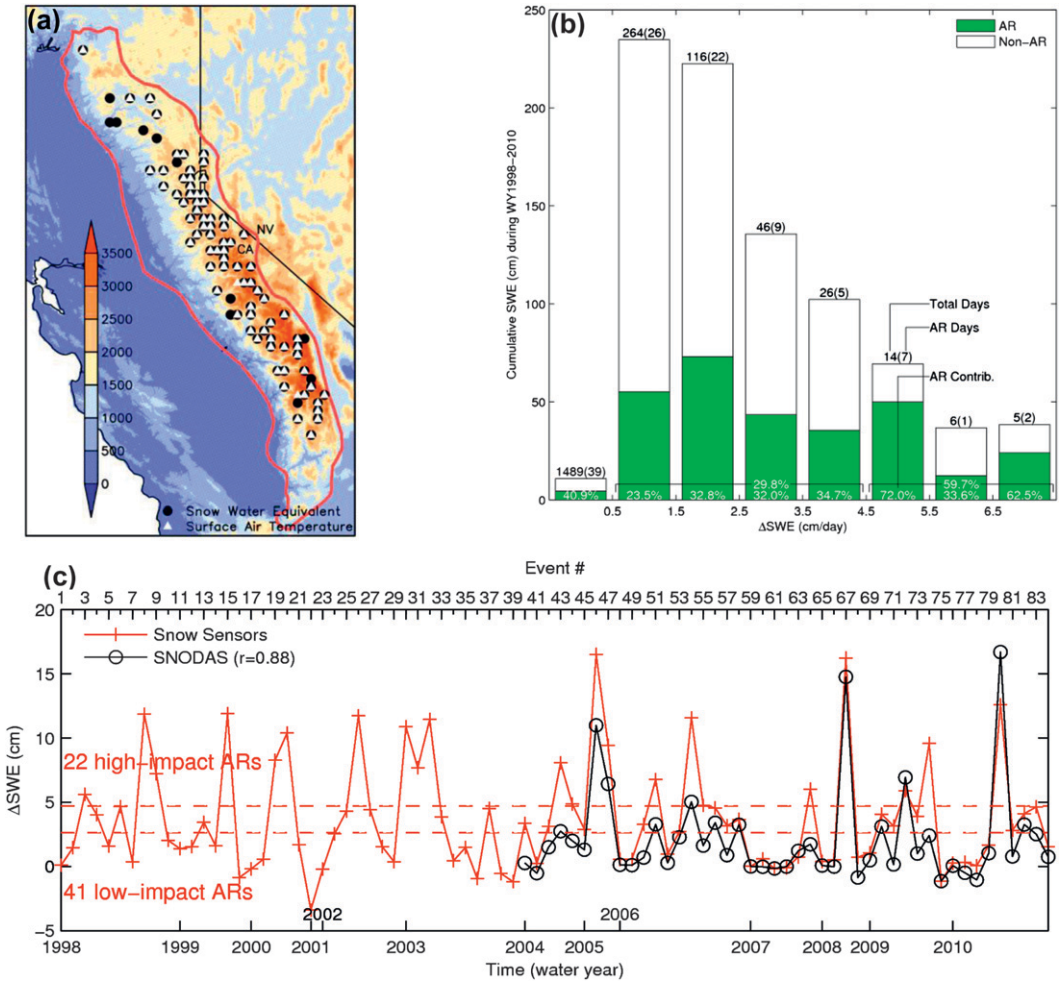


FIG. 1. (a) Elevation (m) map showing the Sierra Nevada domain (red contour) and the snow sensor network (dots). Those sensors with available SAT readings are marked with triangles. (b) The 13-yr (WY 1998–2010) cumulative SWE (cm) in the Sierra Nevada (where elevation is above 1500 m) during the cold-season months (November–March) as a function of daily ΔSWE, with the green (white) bars showing the AR (non-AR) contribution. The total number of dates (AR plus non-AR) and the number of AR dates, within each bin, is indicated on the top of the white bars, outside and inside the brackets, respectively. The percentage contribution of ARs to the cumulative SWE within each bin, and within two groups of bins (0.5–4.5 cm day$^{-1}$, and greater than 4.5 cm day$^{-1}$), is indicated by the white numerals. SWE data are from in situ snow sensor observations. (c) ΔSWE (cm) associated with individual AR events during WY 1998–2010 based on snow sensor observations (plus signs) and SNODAS averaged over all 1 km × 1 km pixels within the Sierra Nevada domain above 1500 m (circles). Correlation between snow sensor and SNODAS ΔSWE is shown in the legend. The dashed lines indicate 1/4 standard deviation above and below the mean snow sensor ΔSWE of the 84 events. ΔSWE is summed from 1 day before to 1 day after an AR event based on daily values.

Hydrologic Remote Sensing Center (NOHRSC), available daily during WY 2004–10 (National Operational Hydrologic Remote Sensing Center 2004).

### *b. Surface air temperature*

Three surface air temperature (SAT) data sources are used: 1) in situ measurements at the snow sensor sites, for which daily means are available from 92 sites (Fig. 1a, triangles) over WY 2006–10; 2) the Atmospheric Infrared Sounder (AIRS) version 5 level 3 standard temperature retrievals (1° × 1° grid; Chahine et al. 2006); and 3) the European Centre for Medium-Range Weather Forecasts (ECMWF) Interim reanalysis 2-m air temperature (1.5° × 1.5° grid; Uppala et al. 2008). Daily means are formed for the latter two products to match in situ observations. For AIRS, the means are weighted averages of the twice-daily satellite passes based on the number of data counts.

### c. Outgoing longwave radiation

Outgoing longwave radiation (OLR) is used as a proxy for tropical convection (large negative OLR anomalies correspond to enhanced convection), as shown in many previous studies (e.g., Graham and Barnett 1987, and references therein). Daily values are available from the National Oceanic and Atmospheric Administration (NOAA) Interpolated OLR product (Liebmann and Smith 1996). For each day, the long-term mean over 1974–2010 is removed to form the OLR anomaly. The 20–100-day filtered OLR anomaly is obtained as follows: interannual variability (such as ENSO) and/or any long-term trend in the OLR anomaly is first removed by subtracting the average over the previous 120 days from each day (Wheeler and Hendon 2004); the daily bandpass-filtered OLR anomaly is then formed by taking the difference between 20- and 100-day running means.

### d. Zonal wind and geopotential height

The 200-hPa zonal wind and geopotential height from the National Centers for Environmental Prediction–National Center for Atmospheric Research (NCEP–NCAR) reanalysis (Kalnay et al. 1996) are used. Daily means are available from 1948, with a 2.5° × 2.5° spatial resolution. Daily anomalies are obtained by removing the long-term mean for each day during 1974–2010.

### e. Madden–Julian oscillation

We use the Real-time Multivariate MJO Index (RMM) introduced by Wheeler and Hendon (2004) to describe the MJO evolution. The index is defined as the leading two principal components from extended EOF analysis of combined daily OLR, 850- and 200-hPa zonal winds along the equatorial band between 15°S and 15°N. The evolution of the MJO is characterized by the eastward propagation of tropical convection from the Indian Ocean to the Western Hemisphere and Africa, and related wind/circulation changes, shown in Fig. 2 for reference. Each MJO phase lasts for a nominal 6-day period. The readers are referred to Wheeler and Hendon (2004) for a detailed accounting of the MJO index and MJO evolution.

### f. Water vapor transport

Daily vertically integrated water vapor transport (IVT) is calculated from specific humidity and vector winds at 12 isobaric levels between 1000 and 100 hPa. Two specific humidity products are used, namely, AIRS version 5 level 3 standard retrievals, and the ECMWF Interim reanalysis; the latter also provides the wind data. IVT is calculated over WY 2003–10 (AIRS data are available from the end of August 2002).

### g. Atmospheric rivers

The AR dates identified by Neiman et al. (2008b) are used. An AR date is when integrated water vapor (IWV) is greater than 2 cm in a region longer than 2000 km and narrower than 1000 km (Ralph et al. 2004), as observed by the Special Sensor Microwave Imager and the Special Sensor Microwave Imager/Sounder. Only those ARs making landfalls along the California coast (i.e., those intersecting the coastline between 32.5° and 41°N) during November–March, the main accumulation period of SWE, are included in this study. We define an AR "event" to be a 1-day or multiday period when each day is an AR date. A total of 84 events are defined over November–March, WY 1998–2010. These events largely occur within a single day period, and rarely exceed 2 days. SWE changes (ΔSWE) calculated for each AR event include 1 day before and 1 day after the event to accommodate for the typical time lead or lag between AR conditions and actual precipitation.

## 3. Sierra Nevada snowpack and atmospheric rivers

The AR focus of this study is spurred by the importance of ARs in extreme hydrological events in the West Coast (Ralph et al. 2006; Neiman et al. 2008a; Ralph et al. 2011). Here, the relative importance of AR versus non-AR events is quantified for our study area. Contribution of AR and non-AR precipitation to the seasonal (November–March) snowpack in the Sierra Nevada is shown in Fig. 1b, expressed as cumulative SWE during WY 1998–2010 as a function of daily ΔSWE. Also shown are the total number of days and the number of AR days for each bin. The overall contribution of ARs to SWE is ~35% during the 13-yr period; a similar number has been reported by Guan et al. (2010) based on SNODAS-assimilated SWE. The rest (~65%) of the SWE is contributed by less intense but more frequent precipitation not related to ARs.[2] The majority (~80%) of the total SWE is contributed by those days with ΔSWE between 0.5 and 4.5 cm day$^{-1}$. About 30% of the SWE accumulated over this daily ΔSWE range is contributed by ARs. The AR percentage contribution doubles for ΔSWE greater than 4.5 cm day$^{-1}$. For the weakest daily ΔSWE range (less than 0.5 cm day$^{-1}$), ARs account for only ~2%–3% of the total number of days, which nonetheless amounts to ~40% of the cumulative SWE over this daily ΔSWE range. The percentage of AR days grows as daily ΔSWE becomes larger. Although the number of AR days

[2] Mean daily ΔSWE during AR events is ~4 times as large as in non-AR events (Guan et al. 2010).

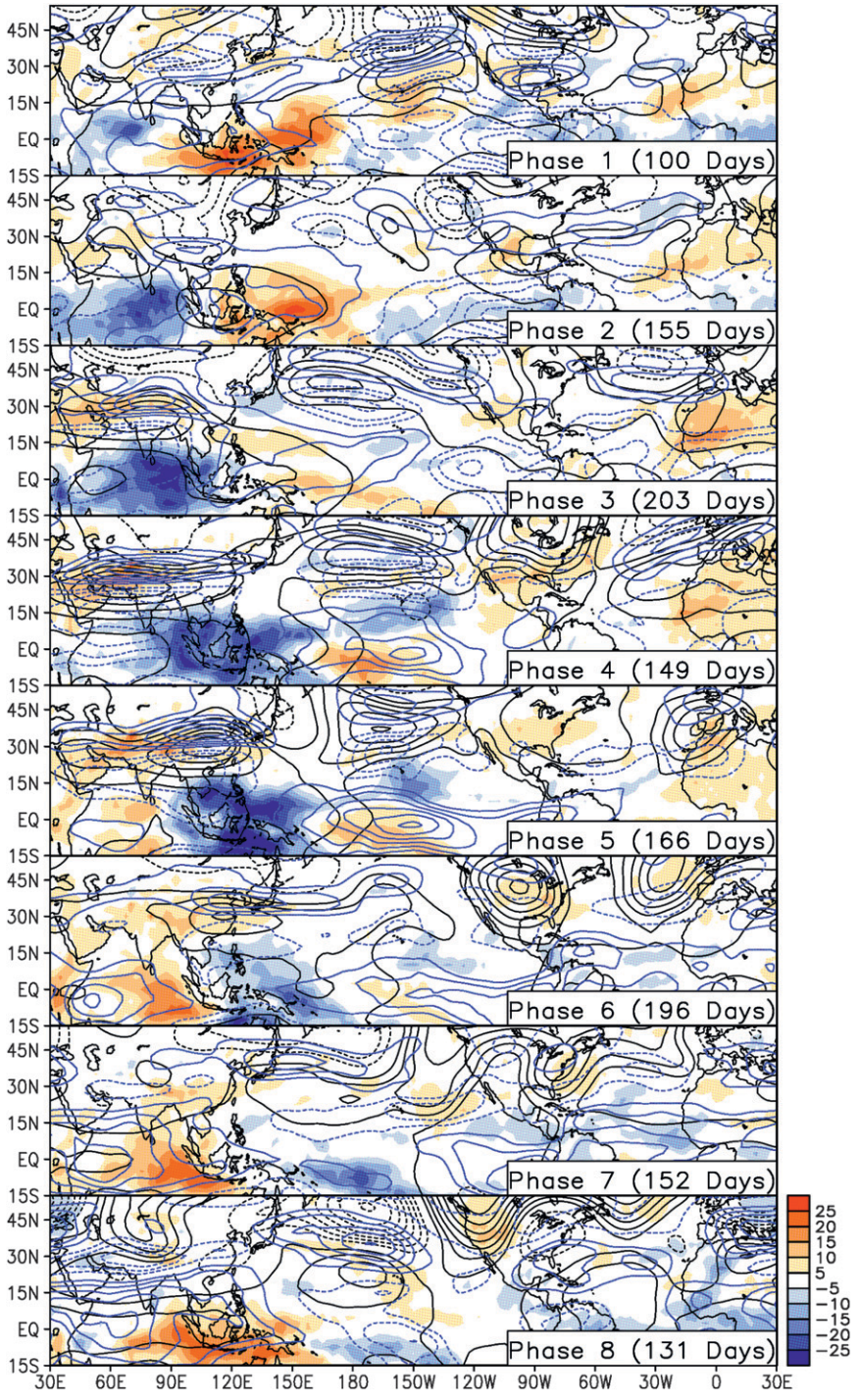


FIG. 2. MJO evolution: Mean anomalies of cold season (November–March) OLR (W $m^{-2}$; shading), 200-hPa zonal wind (m $s^{-1}$; blue contours), and 200-hPa geopotential height (m; black contours) over each MJO phase during WY 1998–2010. Anomalies are relative to the daily climatology for each variable. The contour interval is 2 m $s^{-1}$ for wind and 15 m for geopotential height. Solid (dashed) contours denote positive (negative) values and the zero contours are suppressed. Only strong MJOs (amplitude $\geq$1) are included in the calculation.

never exceeds 50% of the total number of days for any daily ΔSWE range considered, the AR contribution to SWE becomes larger than non-AR contribution when ΔSWE gets larger than 4.5 cm day$^{-1}$. Figure 1b shows that ARs contribute importantly to the seasonal snowpack in the Sierra Nevada, and that the most extreme snow events are more likely associated with ARs.

SWE changes associated with individual AR events during WY 1998–2010 are shown in Fig. 1c (plus signs). Note that the majority of the events (74 out of 84) are associated with positive ΔSWE. Event-to-event variations are large, with the most extreme events resulting in ΔSWE greater than 15 cm, while the weakest events result in negligible changes in SWE. To facilitate subsequent analysis, we define the ''high impact'' AR events (a total of 22) and the ''low impact'' AR events (a total of 41) to be those having ΔSWE at least 1/4 standard deviation above and below the 84-event mean (Fig. 1c, dashed lines), respectively. The threshold is chosen such that the two types of events are well separated and meanwhile a reasonable number of events are retained for each type. The possible relationship between ARs' differing impacts and the MJO is examined in the following section. While not investigated here, it should be noted that ARs can also have high impacts other than by just increasing SWE, such as flooding in particularly warm AR events with very high snow levels.

It is not likely that the magnitude of domain-averaged SWE in the complex terrain in Fig. 1a can be adequately represented by relatively sparse ''point'' observations from the snow sensor sites (Molotch and Bales 2005, 2006). On the other hand, the snow sensor observations show reasonable sensitivities to the event-to-event variations in AR-related snowfall when compared to the much higher-resolution SNODAS product. As seen in Fig. 1c, the snow sensor and SNODAS SWE largely agree with each other (correlation is 0.88) with respect to the relative impact of AR events; there, the SNODAS SWE represents the average over all 1 km × 1 km pixels within the Sierra Nevada domain with elevation greater than 1500 m. The snow sensor SWE is used in subsequent analysis because of the longer data availability period.

## 4. Atmospheric rivers and MJO: Phase relationship

Shown in Fig. 3 is the 200-hPa geopotential height anomaly and the 20–100-day filtered OLR anomaly composited over high- and low-impact ARs, respectively. High-impact ARs are associated with a strong cyclonic anomaly centered northwest of the California coast (Fig. 3a). A strong southwesterly flow anomaly is implied over California. Negative OLR anomalies there are consistent with enhanced convection and precipitation. An interesting band of anomalously low OLR can also be identified in the equatorial western Pacific near 150°E. The cyclonic anomaly associated with low-impact ARs is located farther north and west, and also much weaker in strength (Fig. 3b). OLR anomalies are also much weaker during low-impact ARs in California and in the tropics. Figure 3 suggests that the impact of ARs in California is affected by the meridional location and strength of the AR-bearing extratropical cyclone, which is in turn affected by the background atmosphere. It is likely that tropical convective anomalies associated with the MJO play a considerable role in conditioning the large-scale atmospheric circulation in the extratropics of importance to AR formation and development. Specifically, Fig. 3a suggests that enhanced convection in the equatorial far western Pacific, characteristic of MJO phase 6 (cf. Fig. 2, sixth panel), is associated with high-impact ARs in California. This type of tropical–extratropical linkage is reminiscent of the previous finding by Mo and Higgins (1998) on the connection between long-duration wet/dry spells (on the order of a few weeks) in California and tropical convection.

The relationship between AR activity and the phasing of the MJO is shown in the Wheeler–Hendon diagram in Fig. 4a, where the size of the dots shows the magnitude of AR-related ΔSWE, while the location of the dots indicates the phase of the concurrent MJO. Numerical values are shown for ΔSWE of the high-impact ARs. While almost every MJO phase (the exception being phase 7) has seen a high-impact AR, the most preferred phase appears to be phase 6 (statistical significance is discussed in the following paragraph). Five high-impact ARs occurred during this particular MJO phase, and all five occurred when the MJO was relatively strong (amplitude ≥1). These include the two ARs on 9 January 2005 and 5 January 2008 that produced the largest per event ΔSWE in the Sierra Nevada, and also caused flood-related damages in various parts of California (more information is available online at http://www.cnrfc.noaa.gov and http://www.wrh.noaa.gov). The MJO–AR relationship shown here is consistent with that suggested by Fig. 3 regarding the favorable location of the MJO convection.

To further understand the importance of ARs to extreme snow events, a plot similar to Fig. 4a is made for all dates (AR or non-AR) with ΔSWE greater than 4.7 cm (the same threshold is used to define high-impact ARs) in the Sierra Nevada during November–March, WY 1998–2010. The plot (Fig. 4b) represents the relationship between extreme snow events in the Sierra Nevada and the MJO. As in Fig. 4a, MJO phase 6 stands out as the most favorable for extreme snow events, the majority of which are AR-related. The consistency

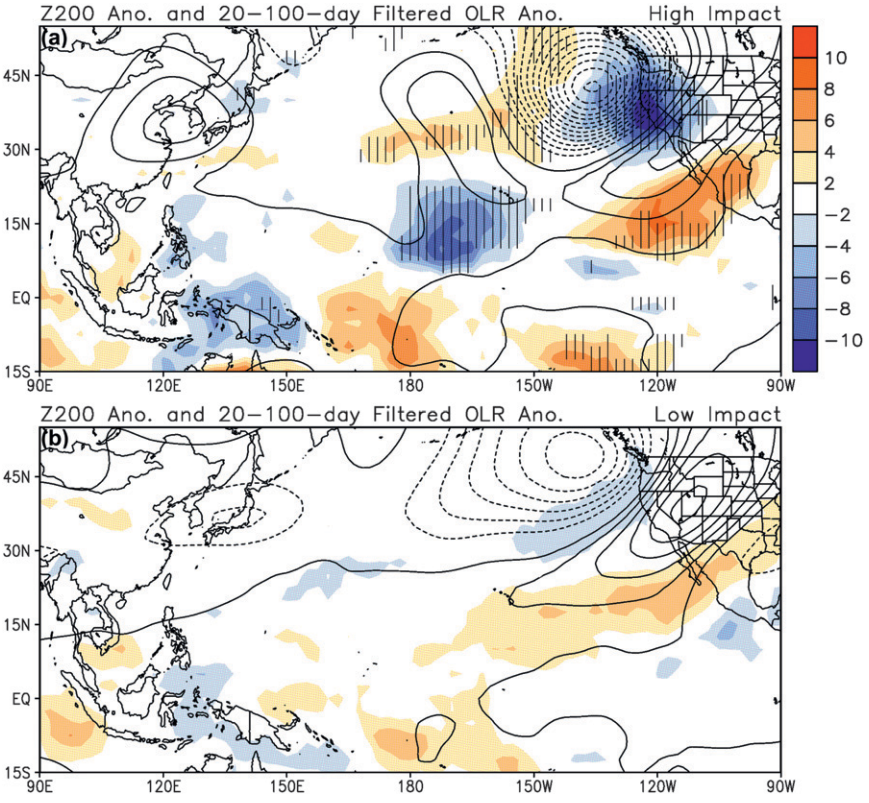


FIG. 3. Mean anomalies of 200-hPa geopotential height (m; contours) and 20–100-day filtered OLR (W $m^{-2}$; shading) over (a) high- and (b) low-impact AR events during WY 1998–2010. Anomalies are relative to the daily climatology for each variable. The contour interval is 20 m for geopotential height, and the zero contour is omitted. Hatching indicates the areas where the difference in the OLR anomaly between (a) and (b) is statistically significant at the 80% level based on the Wilcoxon–Mann–Whitney test.

between Figs. 4a,b suggests that ARs provide a useful framework to understand the impacts of the MJO on extreme snow events.

To assess the significance of the impact of the MJO on AR activity, Monte Carlo simulations are conducted. The AR activity during each MJO phase is defined using three quantities: the number of high-impact AR events, the mean per event ΔSWE over all events (i.e., not just the high-impact ones), and the cumulative ΔSWE over all events. For each quantity, the difference between strong and weak MJOs is tested for statistical significance, as follows. First, all historical wintertime (November–March) MJOs during 1974–2010 are pooled, and 10 000 samples, each with 84 members, are created by random resampling. Then, the difference in the three quantities related to AR activity is calculated between strong and weak MJOs, for each MJO phase, for each sample, forming an empirical distribution of each quantity. The observed value of each quantity is then compared to the 2.5th and 97.5th percentiles based on the empirical distribution. MJO phase 6 is the only phase that passes the significance test for all three quantities and no other phase shows significance for even one of the quantities (Table 1). The agreement between the three test results (all significant) attests to the robustness of the MJO–AR relationship. Bond and Vecchi (2003) explored the impact of MJO on flooding in western Washington and found MJO phases 7 and 6, in this order, to be the most conducive for flooding during the early winter period. Although ARs do not necessarily translate to floods, the close relationship between ARs and floods over some river basins in California (Ralph et al. 2006) calls for further and improved understanding of the MJO–AR relationship in the interest of water resource and flood management in this region.

The MJO–AR relationship identified above can be understood in terms of Rossby wave dynamics. The composite mean upper-tropospheric (200 hPa) circulation anomalies associated with the five high-impact ARs during active MJO phase 6 (see Fig. 4a) is shown in Fig. 5, from 10 days before to the date of AR landfall, at 5-day intervals. Offshore of California, the time evolution

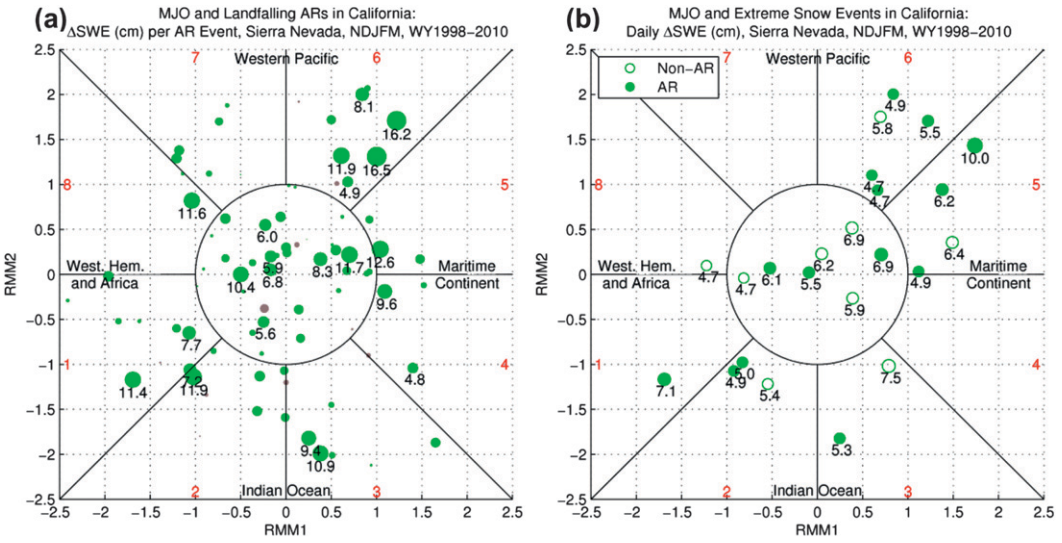


FIG. 4. (a) MJO and landfalling ARs in California on a Wheeler–Hendon diagram: Sierra Nevada ΔSWE (cm) for the 84 AR events during WY 1998–2010 plotted in the MJO space defined by the RMM (Wheeler and Hendon 2004), with the size (i.e., area) of the dots proportional to the magnitude of ΔSWE. Positive values are in green and negative values are in brown. ΔSWE values are also shown in numbers below the dots for the high-impact events. SWE data are from in situ snow sensor observations. Numbers in red (1–8) indicate the MJO phases, and the text labels indicate the geographical location of enhanced convection associated with the MJO phases. (b) As (a), but for all dates (AR or non-AR) with ΔSWE greater than 4.7 cm (i.e., the same threshold as for high-impact ARs) in the Sierra Nevada during November–March, WY 1998–2010. Filled (unfilled) dots indicate ΔSWE related (unrelated) to ARs. ΔSWE is deemed as AR-related if the 3-day period centered on the current day contains at least one AR date.

is marked by the arrival of a strong extratropical cyclone that evolved from a trough observable 5 days earlier to the west. A moisture tongue with above 2 cm integrated water vapor is well developed south of the extratropical cyclone on the date of AR landfall. Enhanced moisture and wind speed contribute to focused and terrain-perpendicular water vapor fluxes toward the coastal and inland mountains of California. Over the tropics, negative OLR anomalies are seen over the Maritime Continent 10 days before AR landfall, which move to the western Pacific 10 days later. Associated with the tropical convective anomalies are perturbations in the large-scale atmospheric circulation, characterized by an upper-tropospheric wave train extending from East Asia to North America. An eastward transport of wave energy is suggested. The development of the AR-bearing extratropical cyclone is accompanied by the eastward extension of strong westerly jet-stream winds, consistent with the impact of MJO on high-frequency transients through modulation of the waveguiding Pacific jet (Matthews and Kiladis 1999).

The circulation pattern associated with high-impact MJO phase 6 ARs (Fig. 5c) is expectedly different from the climatological MJO phase 6 circulation pattern (Fig. 2, sixth panel), because the five ARs only account for a few percent of the total number of days (i.e., 196) associated with this MJO phase. In this regard, the MJO, and likely other low-frequency variability in the ocean and atmosphere (such as ENSO and the Pacific–North American teleconnection pattern), only acts to modulate the large-scale background on which the high-frequency transients evolve. The formation and impact of an

TABLE 1. The impact of MJO on AR activity, measured by the difference in three quantities between strong and weak MJOs for each MJO phase during WY 1998–2010: 1) high-impact AR count, 2) mean per event ΔSWE (cm), and 3) cumulative ΔSWE (cm). Italic values are significant at the 95% level based on Monte Carlo simulations.

| | | MJO phase | | | | | | | |
|---|---|---|---|---|---|---|---|---|---|
| | | 1 | 2 | 3 | 4 | 5 | 6 | 7 | 8 |
| Diff between strong and weak MJOs | High-impact AR count | 2 | 1 | 2 | 2 | −1 | *5* | −2 | 0 |
| | Mean per event ΔSWE | 3.3 | 2.9 | 0.1 | 3.4 | 1.8 | *6.2* | −2.0 | 3.3 |
| | Cumulative ΔSWE | 28.7 | 29.9 | 19.1 | 14.3 | −12.4 | *58.0* | −7.7 | −4.7 |

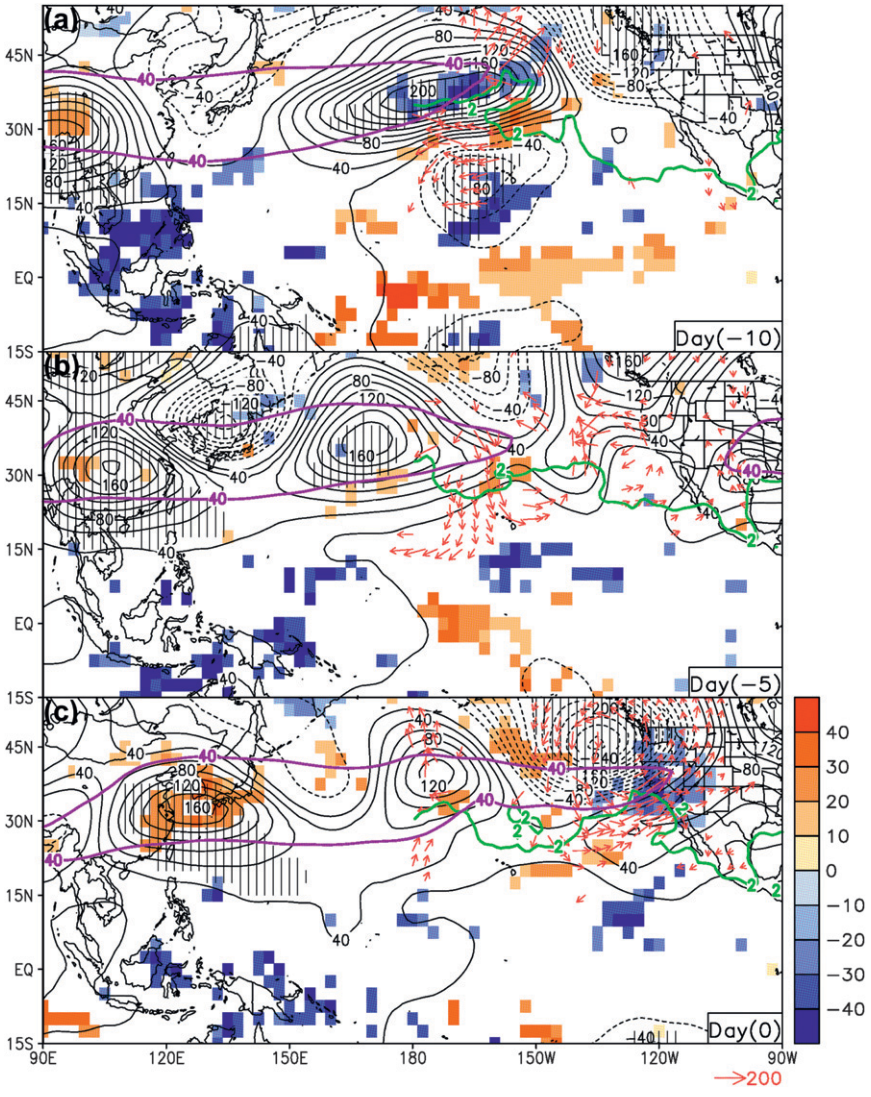


FIG. 5. Mean anomalies of OLR (W $m^{-2}$; shading) and 200-hPa geopotential height (m; black contours) composited over the five high-impact ARs during active MJO phase 6 (see Fig. 4a), from (a) 10 days before landfall, (b) 5 days before landfall, to (c) the date of landfall. The zero contour is suppressed for geopotential height. Superposed is the 40 m $s^{-1}$ contour of the 200-hPa total zonal wind (purple), the 2-cm contour of the total IWV (green), and the vectors of IVT anomaly (red). Anomalies are relative to the daily climatology for each variable. OLR and IVT are shown only for values statistically significant at the 95% level. Hatching indicates geopotential height values significant at the 95% level. IWV and IVT are shown only for the area east of the date line and north of 15°N.

actual AR depends on many conditions and processes, understanding of which is being rapidly improved through data analysis, modeling, and dedicated field campaigns.

The concurrent MJO–AR relationship identified above provides a potential tool to "diagnose" AR activity during a developing and/or evolving MJO event, or develop outlooks of AR activity given that useful forecasts of the MJO can be made empirically at a 2–3-week lead (Waliser 2006; Jiang et al. 2008). A related question is whether the MJO–AR relationship in Fig. 4a is maintained when a time lag is introduced. To address this question, Fig. 4a is regenerated with the MJO leading the ARs by 10 days (not shown). The robustness of the time-lagged relationship is then assessed using procedures similar to those in Table 1. No consistent relationship is found between AR activity and the phase of the MJO 10 days earlier. This is understandable,

because each MJO phase may last for a different period of time, and the phase evolution can be somewhat irregular, such that the AR-preferred MJO phase (i.e., phase 6) is not preceded by a particular MJO phase 10 days earlier. This means that predictive skills on AR activity derived from the above MJO–AR relationship is limited by the predictive skill of the MJO itself.

## 5. Atmospheric rivers and MJO: Seasonality

The timing of big winter storms is important from a hydrological and water management standpoint. Significant snow accumulation during the late season is helpful in alleviating water supply shortfalls. Here, we explore the relationship between the timing of AR and the MJO. The monthly distribution of the 84 AR events is shown in Fig. 6a. Eighteen out of the 22 high-impact events occurred during December–February; the other 4 occurred in November and March. The majority of the high-impact ARs are associated with strong MJOs during most of their months of occurrence. The reverse statement is not true, though, as can be expected: only 15 AR events occurred during the total of 1252 strong MJO days.

We categorize each water year based on the date when the first high-impact AR occurred during the winter season. Seven (five) water years see their first high-impact AR on or before (after) 15 January, referred to here as the ''early-winter impact'' (''late-winter impact'') years. No high-impact AR occurred in WY 2001, which is not included in this analysis. Mean 20–100-day filtered OLR anomalies, averaged between 15°S and 15°N, are shown in Figs. 6b,c for the two categories of years. The early-winter impact years are marked by a propagation of negative OLR anomalies starting from the western Indian Ocean in early December, and reaching the western Pacific in early January while gaining and maintaining strengths. In comparison, the late-winter impact years are characterized by enhanced negative OLR anomalies over the eastern Indian Ocean in late December, which weaken and lose identity as they reach the western Pacific around mid-January, and then redevelop near the date line in late January. The difference in the timing and location of the OLR minimum suggests a likely impact of MJO on the timing of high-impact ARs during the cold season. However, more years of data are needed for a more robust assessment (note that the values shown in Fig. 6 are significant at a marginal 80% level).

## 6. MJO modulation of seasonal snowpack

The relationship between MJO and seasonal snowpack in the Sierra Nevada is examined in Fig. 7. In this case only consideration of MJO phase is made, while distinguishing between AR and non-AR events is not considered. This allows the effects of the less intense, but more frequent non-AR events (cf. AR events) to be factored in, implicitly. For each MJO phase, the mean daily ΔSWE anomaly during November–March, relative to the seasonal mean (Fig. 7i), is calculated. Statistical significance is evaluated based on Monte Carlo simulation. The discussion here focuses on statistically significant features (shown in dark colors in Figs. 7a–h). The positive (negative) ΔSWE anomaly is seen most prominent during MJO phase 3 (8), which spans a large fraction of the Sierra Nevada domain (Figs. 7c,h). The near-symmetry between the two phases is interesting. The ΔSWE anomalies are roughly half the seasonal mean over many sites, with absolute values being as large as 0.4–0.5 cm $day^{-1}$. The magnitude of MJO modulation on ΔSWE is comparable to the finding by Bond and Vecchi (2003) on winter precipitation in western Washington and Oregon, although the MJO phases with the highest impact differ. ΔSWE anomalies are in general weaker and/or distributed over more limited areas for other MJO phases, including MJO phase 6, the only phase during which AR activity is significantly increased, as discussed above. This suggests that MJOs affect AR and non-AR snow accumulation in different ways, which is worth further investigation. Latitudinal preference of impact is notable for some MJO phases, such as the predominant southern Sierra Nevada impact associated with MJO phases 5 and 7, and the largely northern Sierra Nevada impact associated with MJO phase 6. We emphasize here that the phase relationship in Fig. 7 reflects the climatological mean. Over a given MJO cycle, the relationship can be modified by variations in solar insolation, melting level height, and other factors that may affect the amount of accumulated snow.

To look into some of the physical processes involved in Fig. 7, similar composites are made for SAT anomalies based on the in situ data, shown in Fig. 8. A negative relationship can be identified between SAT and ΔSWE during MJO phases 3 and 8; phase 3 (8) showing cold (warm) SAT anomalies (Figs. 8c,h), accompanied by above-average (below-average) ΔSWE (Figs. 7c,h). The underlying SAT and ΔSWE relationship is consistent with Guan et al. (2010), who showed a crucial role of SAT in determining AR-related snow accumulation. In principal, warm air temperatures favor high-precipitation winter storms with increased atmospheric capacity for moisture. On the other hand, warm air temperatures (higher melting levels) are unfavorable for orographically forced snowfall. The actual impact of air temperature on snow amount depends, in part, on the balance between the above two effects. Compared to MJO phases 3 and 8, other MJO phases with generally weaker SAT anomalies show

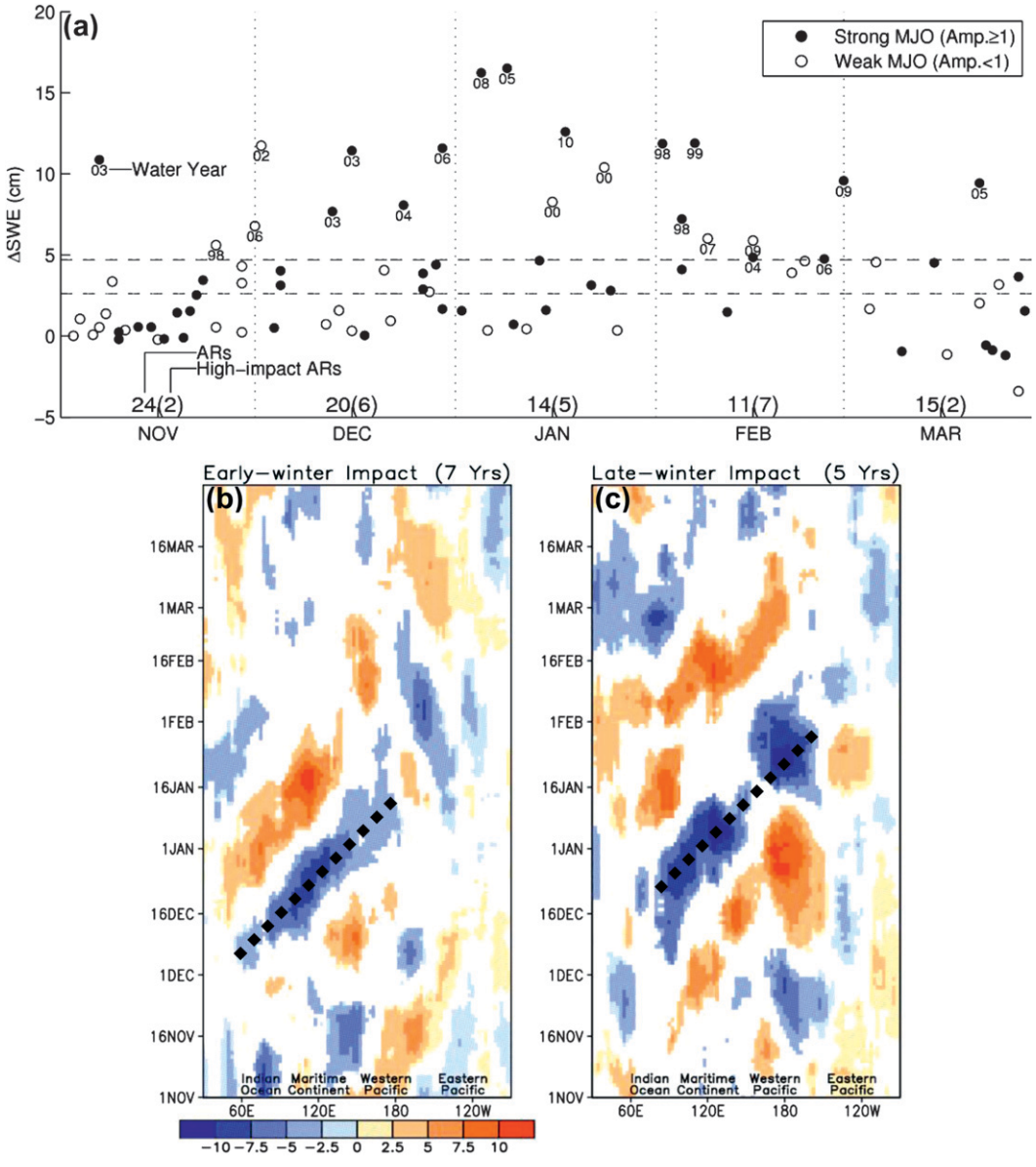


FIG. 6. (a) ΔSWE (cm) associated with individual AR events during WY 1998–2010 (as in Fig. 1c, plus signs): seasonal distribution. The horizontal dashed lines indicate 1/4 standard deviation above and below the mean ΔSWE of the 84 events. The vertical dotted lines mark the beginning of each calendar month. (b),(c) Mean 20–100-day filtered OLR (W $m^{-2}$) anomalies (relative to a daily climatology) composited over the water years during which the first high-impact AR event occurred on or before 15 Jan and after 15 Jan, respectively, averaged between 15°S and 15°N. Only values significant at the 80% level are shown. The thick dashed lines mark the propagation of low OLR discussed in the text.

less coherent relationships between SAT and ΔSWE; the SAT–ΔSWE decoupling over many sites suggests other processes are in effect in determining snow amount.

The SAT composites in Fig. 8 are compared to satellite and reanalysis data to evaluate the representation of the MJO effect in these data products. The comparison is focused on MJO phases 3 and 8, during which the observed SAT anomalies are relatively large and the SAT–ΔSWE relationship is most coherent. The contrasting SAT patterns between MJO phases 3 and 8 in in situ observations are found in both AIRS (Figs. 9a,b) and ECMWF Interim reanalysis (Figs. 9c,d) data. The overall similarity between the latter two data products, especially over the oceans, is attributable to the assimilation of AIRS temperature profiles in the reanalysis. On the other hand, the magnitude of the overland SAT anomalies is more

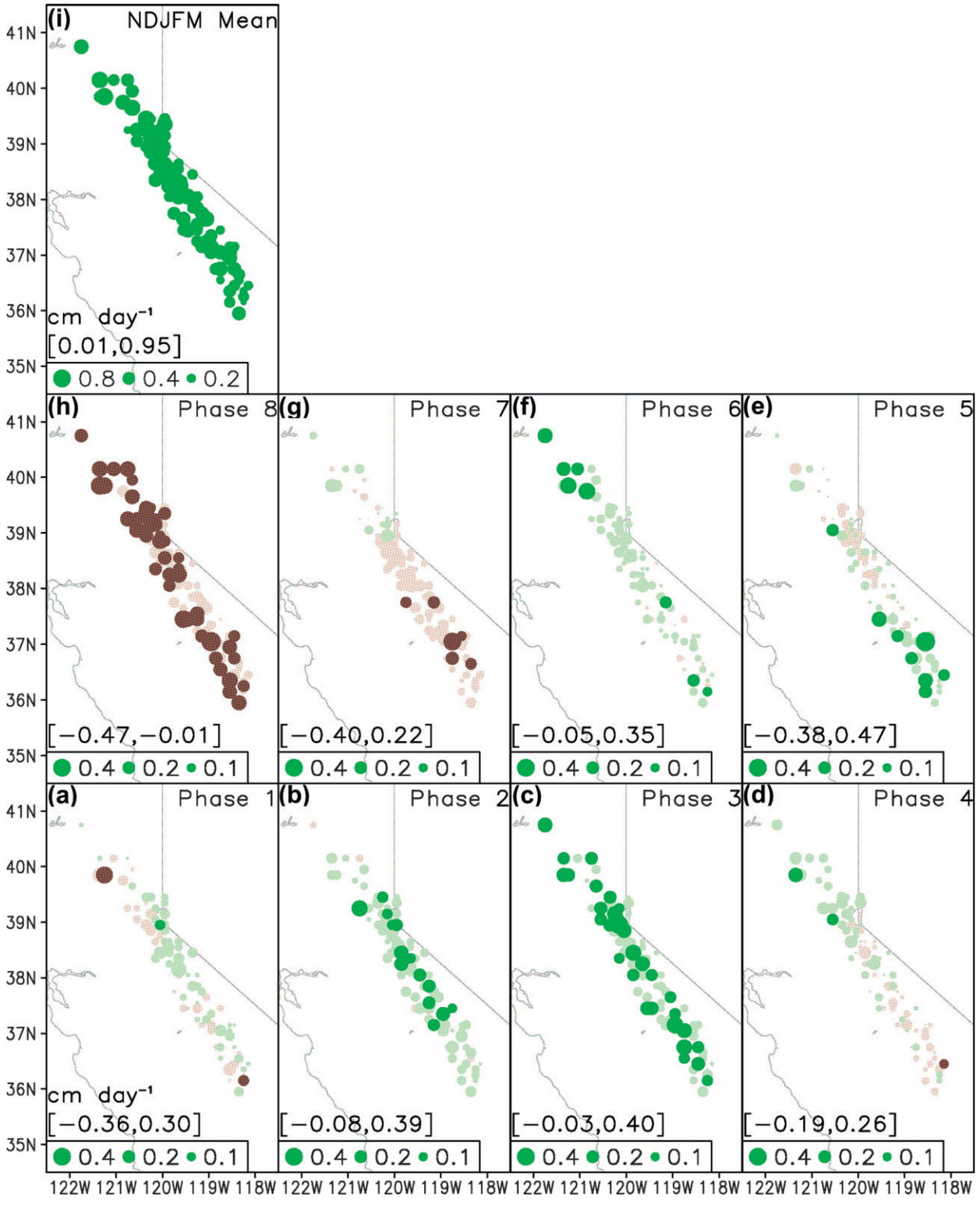


FIG. 7. (a)–(h) Mean daily ΔSWE (cm day$^{-1}$) anomaly relative to the cold-season (November–March) mean composited over each MJO phase during WY 1998–2010. Only strong MJOs (amplitude ≥1) are included in the calculation. The eight MJO phases are plotted counterclockwise, with the bottom left being phase 1. Positive numbers are in green and negative values are in brown. The range of the values is shown in square brackets. Dark colors indicate statistical significance at the 95% level based on Monte Carlo simulation. (i) Mean daily ΔSWE (cm day$^{-1}$) during the cold season.

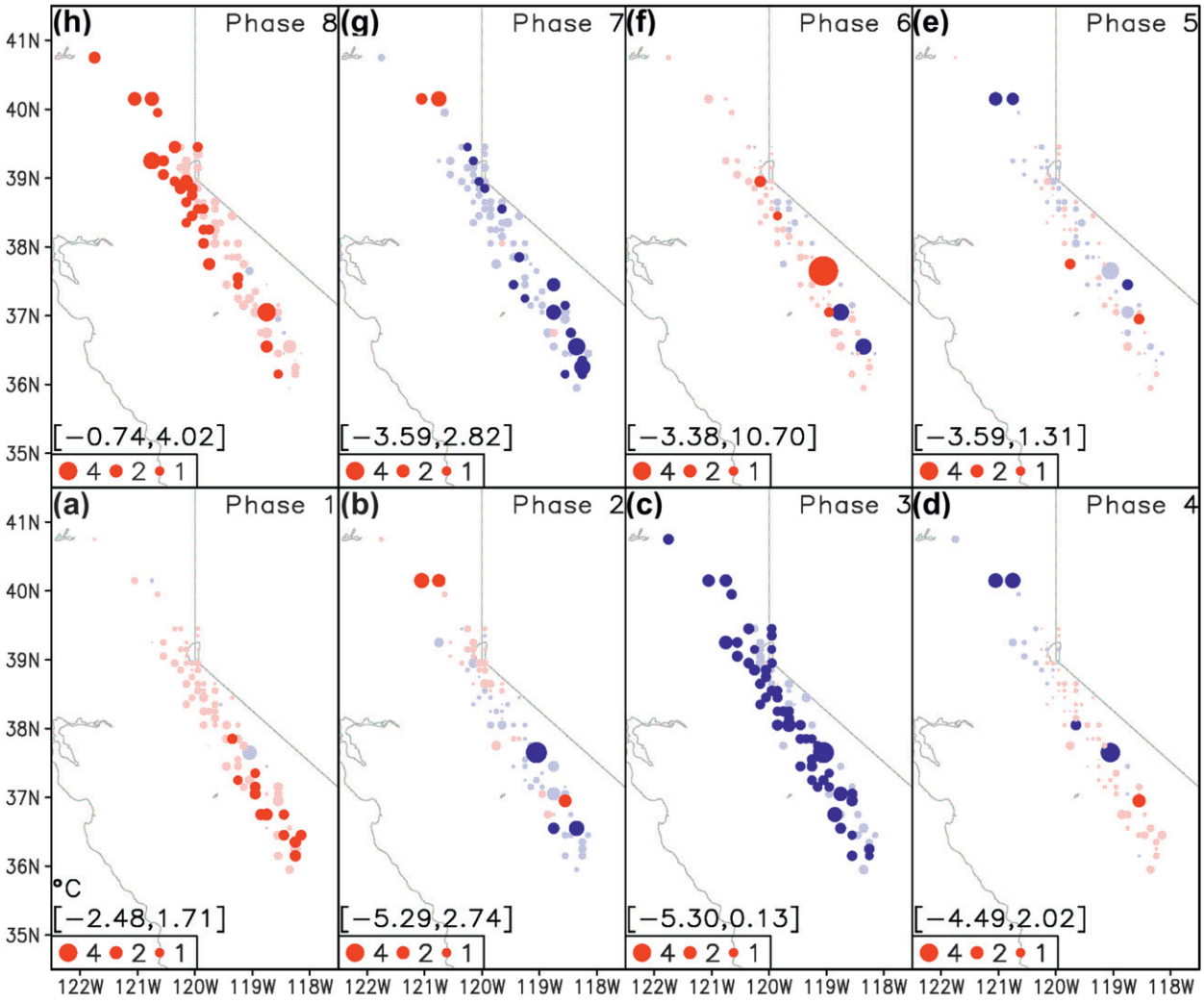


FIG. 8. (a)–(h) Mean SAT (°C) anomaly relative to the cold-season mean composited over each MJO phase during WY 2006–10. Positive numbers are in red and negative values are in blue. The rest is as in Figs. 7a–h.

realistic in AIRS than in the reanalysis (AIRS being larger by approximately a factor of 2), using in situ observations from Fig. 8 as a reference.

Water vapor transported from the Pacific Ocean provides the bulk of moisture for orographic precipitation in the coastal and inland mountains of California, including in the cases of ARs. Both the direction (relative to the mean mountain topography) and the strength of the water vapor flux affect the amount of incoming moisture available for precipitation (Alpert 1986; Pandey et al. 1999). To examine the effect of the MJO in this regard, composite maps for the IVT anomalies for each MJO phase are shown in Figs. 10 and 11, based on water vapor data from AIRS and ECMWF Interim reanalysis, respectively. Utilization of two water vapor products provides the cross corroboration needed given the lack of in situ data for comparison. Wind data are from the reanalysis in both figures. The two figures show overall similar IVT anomaly patterns. The discussion below focuses on common features of the two figures. Dramatically different IVT patterns are found between MJO phases 3 and 8, during which ΔSWE anomalies are most prominent and with opposite signs. Positive ΔSWE anomalies in MJO phase 3 are accompanied by an IVT band directed eastward toward California, with a considerable terrain-perpendicular component. IVT in the tropics and subtropics is directed westward (away from the coast) during this MJO phase. The direction of IVT is largely reversed during MJO phase 8. In this case, tropical/subtropical moisture is transported poleward over the northeastern Pacific. Close to California, the IVT is directed away from the mountain topography, which then joins the largely northward IVT away from the coast. The different source region of the airstream

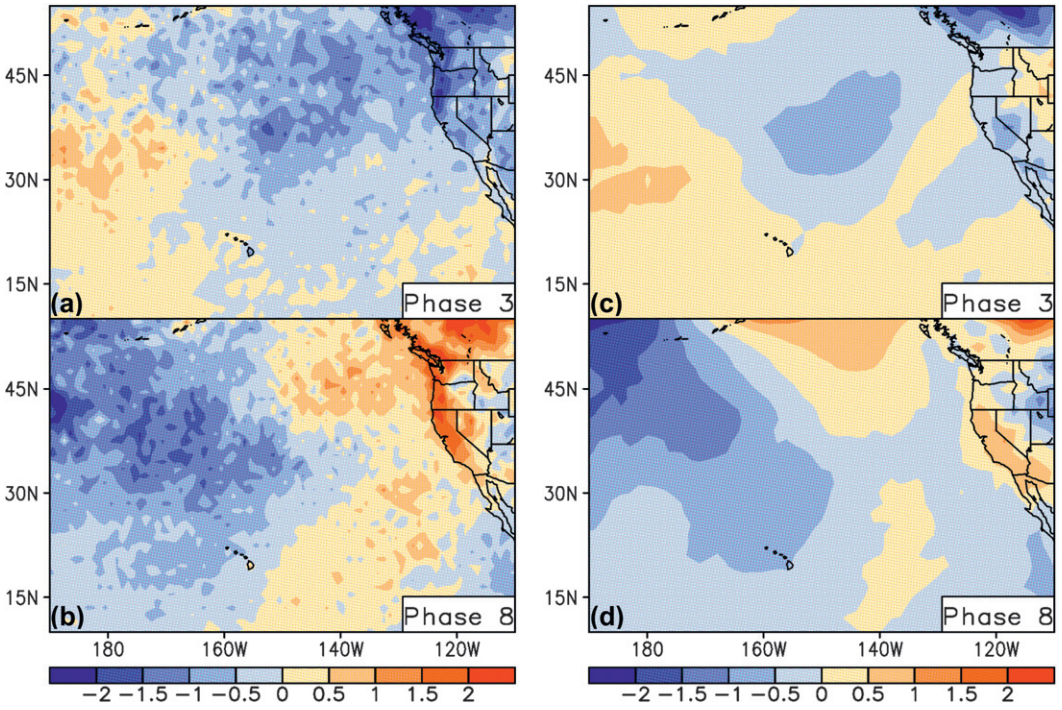


FIG. 9. (a),(b) Mean SAT (°C) anomaly relative to the cold-season mean composited over MJO phases 3 and 8 during WY 2006–10, with SAT data from AIRS satellite retrievals. Only strong MJOs (amplitude ≥1) are included in the calculation. (c),(d) As in (a),(b), but for SAT data from the ECMWF Interim reanalysis.

impacting California between MJO phases 3 and 8 (i.e., relatively cold air from the Gulf of Alaska as opposed to much warmer air from the tropics/subtropics) is consistent with the accompanying SAT anomaly patterns (see Figs. 8 and 9). IVT anomalies associated with the other MJO phases are much weaker or insignificant in the California area. The IVT and ΔSWE patterns shown here are consistent with orographic enhancement of winter precipitation in the Sierra Nevada through MJO modulation of the seasonal mean circulation and associated moisture transport.

Some differences can nonetheless be identified between Figs. 10 and 11, which should be attributed to the different water vapor data used in the calculation of the IVT. Compared to AIRS, the ECMWF Interim reanalysis indicates a slightly larger water vapor content. This is consistent with Tian et al. (2010), who showed that MJO-related water vapor anomalies are larger by ~20% in the ECMWF Interim reanalysis than in AIRS in the free troposphere.

## 7. Conclusions

The importance of the MJO to the Sierra Nevada snowpack is established through analysis of the relationship between the phasing of the MJO, the intensity and seasonality of landfalling ARs, and related SWE changes, based on a collection of in situ, satellite, and reanalysis data products during WY 1998–2010.

The relative magnitude of AR and non-AR snow accumulation suggests the dominance of ARs in the most extreme snow events. For events with daily ΔSWE between 0.5–4.5 cm, the AR contribution to SWE is ~30%. The percentage doubles for events with daily ΔSWE greater than 4.5 cm. Taken together, ARs contributed ~35% of the total SWE during the 13 winters (November–March).

AR activity in California, as measured by the number of high-impact ARs, mean per event ΔSWE, and the cumulative ΔSWE (the latter two are measured over all ARs irrespective of impact), is significantly affected by the MJO. The three quantities are all larger (at the 95% significance level) when MJO is active (amplitude ≥1) over the far western tropical Pacific (i.e., during MJO phase 6 based on the Wheeler–Hendon index). Over the 13-yr analysis period, five high-impact ARs occurred during this particular phase of the MJO when it was active, including the largest two events on 9 January 2005 and 5 January 2008. The MJO also shows considerable modulation of the seasonality of ARs: those years with the first

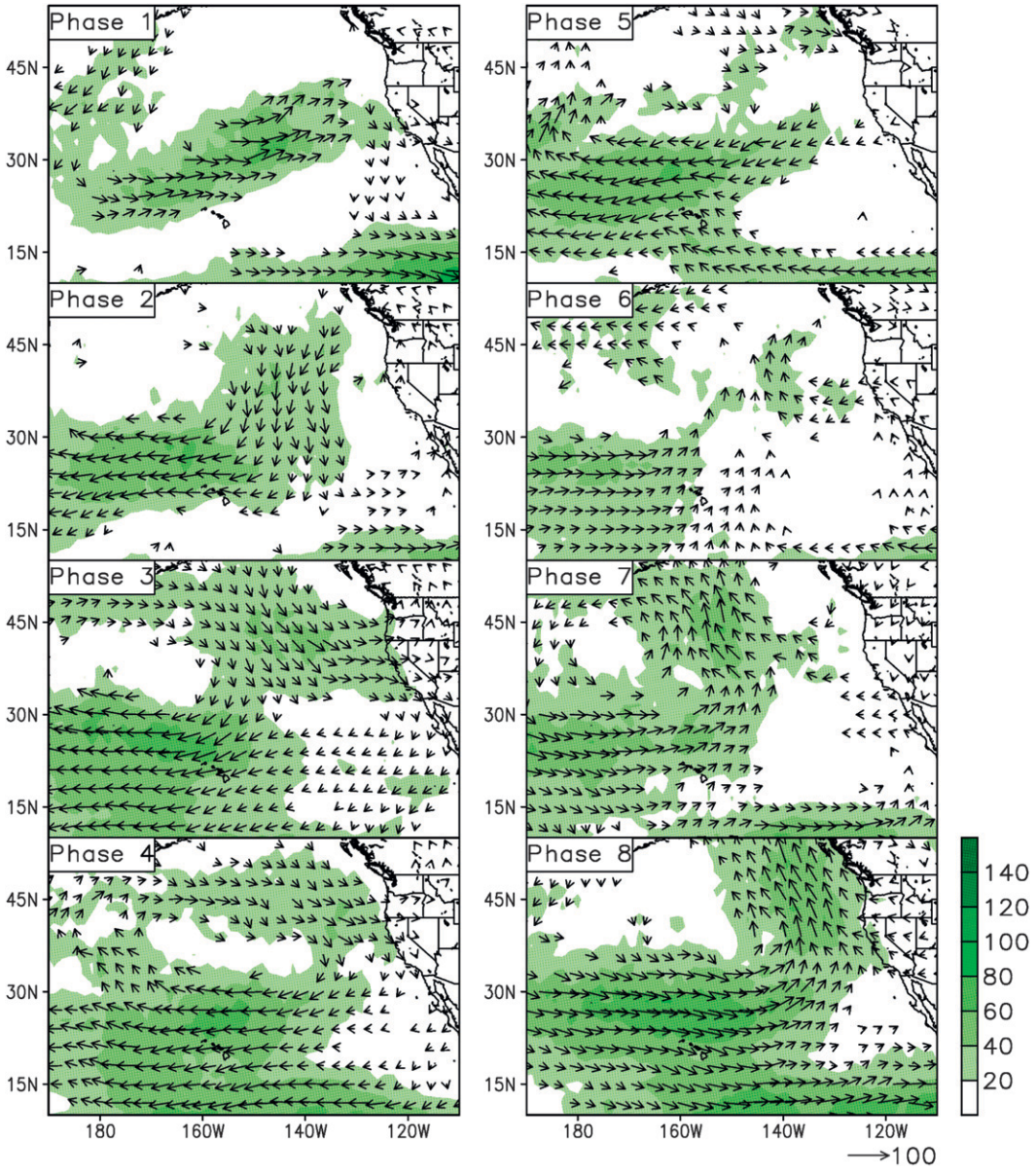


FIG. 10. IVT (kg $m^{-1}$ $s^{-1}$) anomaly relative to the cold-season mean composited over each MJO phase during WY 2003–10. Only strong MJOs (amplitude $\geq 1$) are included in the calculation. Shading shows the magnitude, and the vectors show the direction/magnitude where statistically significant at the 95% level. Water vapor data are from AIRS satellite retrievals and wind data are from the ECMWF Interim reanalysis.

occurrence of a high-impact AR after 15 January (i.e., during the latter half of the cold season) are accompanied by convective anomalies propagating to the tropical western Pacific a few weeks later than the other years.

Total snow accumulation in the Sierra Nevada is most significantly modified during MJO phases 3 (active convection over the eastern Indian Ocean) and 8 (active convection over the Western Hemisphere), with opposite effects: positive and negative ΔSWE anomalies span a large fraction of the Sierra Nevada domain during these two MJO phases, respectively, with the magnitude of the daily anomaly being roughly half the cold-season mean daily ΔSWE over many sites and the absolute values being as large as 0.4–0.5 cm $day^{-1}$. The positive (negative) ΔSWE anomaly is accompanied by cold (warm) SAT anomaly and onshore (offshore) IVT anomaly. The contrasting SAT patterns associated with MJO phases 3 and 8, revealed by the in situ observations, are more realistically represented in AIRS satellite retrievals than in the ECMWF Interim reanalysis.

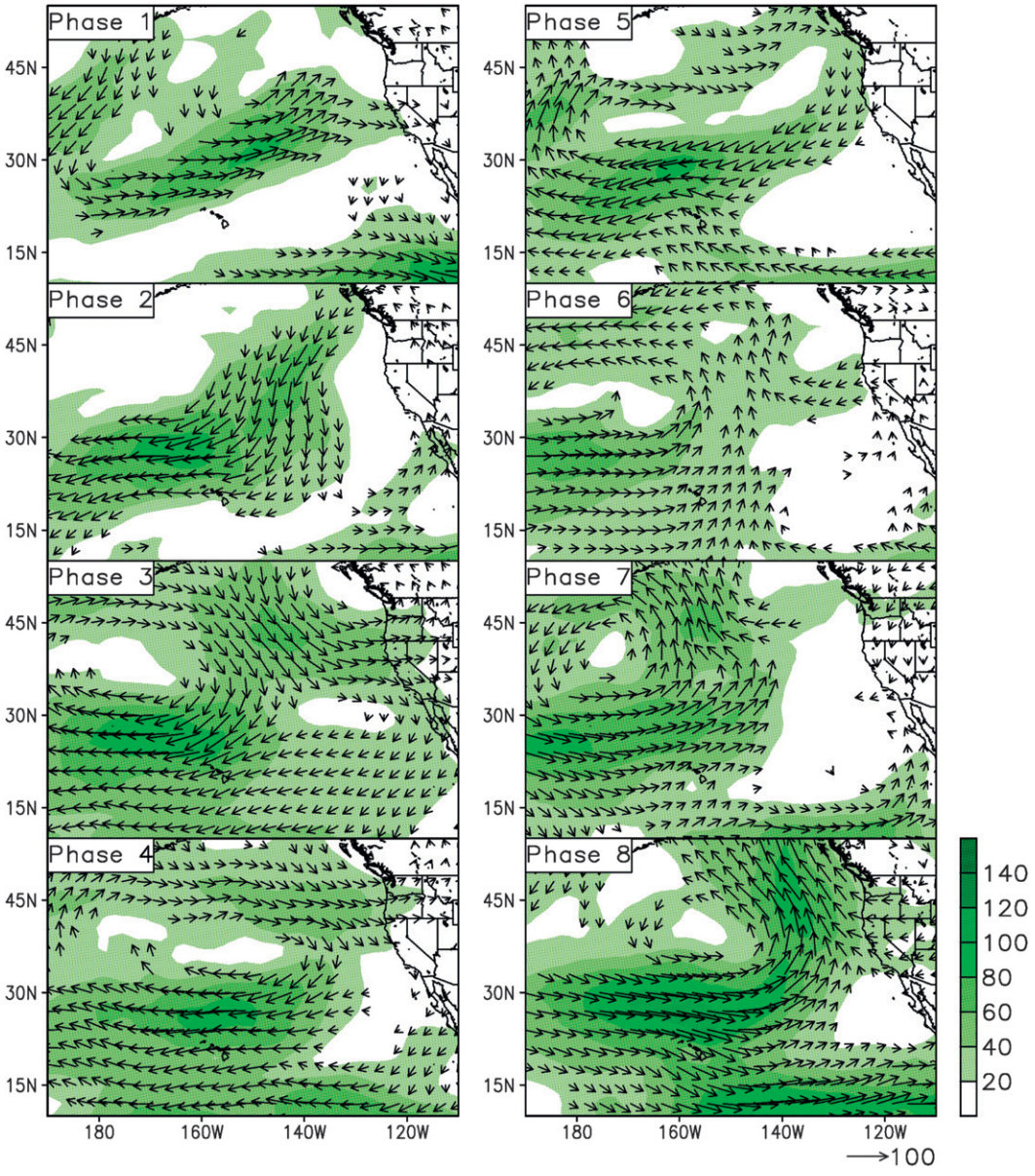


FIG. 11. As in Fig. 10, but for water vapor data from the ECMWF Interim reanalysis.

The close relationship between the MJO and the Sierra Nevada snowpack, part of which is through MJO's impact on big winter storms related to ARs, has broad implications to weather, hydrology, and water resources in California and other water-stressed western states, currently and in the future. A recent study showed earlier melting of the Sierra Nevada snowpack in response to warming temperatures in the recent few decades (Kapnick and Hall 2010), which is likely to continue or accelerate given projected surface warming in this region. The frequency of MJOs is likely to increase in a warming climate (Jones and Carvalho 2011), as is the frequency of landfalling ARs in California (Dettinger 2011). These would add to the vulnerability of the Sierra Nevada snowpack to projected climate change, since AR storms are relatively warm with the snow–rain partitioning sensitive to small perturbations in temperature. With more precipitation falls during extreme events (ARs) and/or as rain, the challenge for water and flood management becomes larger. Improved forecasts and prediction of winter storm activities and related snowpack changes on a range of time scales are critical for meeting this challenge. Our ability to do so relies upon continued observational and modeling efforts regarding MJO, AR, and mountain snowpack.

*Acknowledgments.* This research was supported by NASA Grant NNX08AH18G, NSF Grant EAR 1032295, and by ARRA funds. Additional support was provided by the Water Resources Area of the NASA Applied Sciences Program. Thanks go to K. Weickmann, R. Wood, P. Webster, I.-S. Kang, J. Wallace, and G. Kiladis for helpful discussions and comments; and to F. Ralph for his encouragement. DEW's, EJF's, and BG's contribution, and part of NPM's contribution, to this study were carried out on behalf of the Jet Propulsion Laboratory, California Institute of Technology, under a contract with the National Aeronautics and Space Administration.

## REFERENCES

Alpert, P., 1986: Mesoscale indexing of the distribution of the orographic precipitation over high mountains. *J. Climate Appl. Meteor.,* **25,** 532–545.

Bales, R. C., N. P. Molotch, T. H. Painter, M. Dettinger, R. Rice, and J. Dozier, 2006: Mountain hydrology of the western United States. *Water Resour. Res.,* **42,** W08432, doi:10.1029/2005WR004387.

Bond, N. A., and G. A. Vecchi, 2003: The influence of the Madden–Julian Oscillation on precipitation in Oregon and Washington. *Wea. Forecasting,* **18,** 600–613.

Chahine, M. T., and Coauthors, 2006: AIRS: Improving weather forecasting and providing new data on greenhouse gases. *Bull. Amer. Meteor. Soc.,* **87,** 911–926.

Dettinger, M. D., 2011: Climate change, atmospheric rivers and floods in California—A multimodel analysis of storm frequency and magnitude changes. *J. Amer. Water Resour. Assoc.,* **47,** 514–523, doi:10.1111/j.1752-1688.2011.00546.x.

——, F. M. Ralph, T. Das, P. J. Neiman, and D. R. Cayan, 2011: Atmospheric rivers, floods, and the water resources of California. *Water,* **3,** 445–478, doi:10.3390/w3020445.

Graham, N. E., and T. P. Barnett, 1987: Sea surface temperature, surface wind divergence, and convection over tropical oceans. *Science,* **238,** 657–659, doi:10.1126/science.238.4827.657.

Grubišić, V., R. K. Vellore, and A. W. Huggins, 2005: Quantitative precipitation forecasting of wintertime storms in the Sierra Nevada: Sensitivity to the microphysical parameterization and horizontal resolution. *Mon. Wea. Rev.,* **133,** 2834–2859.

Guan, B., N. P. Molotch, D. E. Waliser, E. J. Fetzer, and P. J. Neiman, 2010: Extreme snowfall events linked to atmospheric rivers and surface air temperature via satellite measurements. *Geophys. Res. Lett.,* **37,** L20401, doi:10.1029/2010GL044696.

Hayes, P. S., L. A. Rasmussen, and H. Conway, 2002: Estimating precipitation in the central Cascades of Washington. *J. Hydrometeor.,* **3,** 335–346.

Higgins, R. W., and K. C. Mo, 1997: Persistent North Pacific circulation anomalies and the tropical intraseasonal oscillation. *J. Climate,* **10,** 223–244.

Jiang, X., D. E. Waliser, M. C. Wheeler, C. Jones, M.-I. Lee, and S. D. Schubert, 2008: Assessing the skill of an all-season statistical forecast model for the Madden–Julian oscillation. *Mon. Wea. Rev.,* **136,** 1940–1956.

Jones, C., 2000: Occurrence of extreme precipitation events in California and relationships with the Madden–Julian Oscillation. *J. Climate,* **13,** 3576–3587.

——, and L. M. V. Carvalho, 2011: Will global warming modify the activity of the Madden–Julian Oscillation? *Quart. J. Roy. Meteor. Soc.,* **137,** 544–552, doi:10.1002/qj.765.

——, D. E. Waliser, K. M. Lau, and W. Stern, 2004: Global occurrences of extreme precipitation and the Madden–Julian Oscillation: Observations and predictability. *J. Climate,* **17,** 4575–4589.

Kalnay, E., and Coauthors, 1996: The NCEP/NCAR 40-Year Reanalysis Project. *Bull. Amer. Meteor. Soc.,* **77,** 437–471.

Kapnick, S., and A. Hall, 2010: Observed climate–snowpack relationships in California and their implications for the future. *J. Climate,* **23,** 3446–3456.

Leung, L. R., and Y. Qian, 2009: Atmospheric rivers induced heavy precipitation and flooding in the western U.S. simulated by the WRF regional climate model. *Geophys. Res. Lett.,* **36,** L03820, doi:10.1029/2008GL036445.

Liebmann, B., and C. A. Smith, 1996: Description of a complete (interpolated) outgoing longwave radiation dataset. *Bull. Amer. Meteor. Soc.,* **77,** 1275–1277.

Matthews, A. J., and G. N. Kiladis, 1999: The tropical–extratropical interaction between high-frequency transients and the Madden–Julian Oscillation. *Mon. Wea. Rev.,* **127,** 661–677.

Mo, K. C., and R. W. Higgins, 1998: Tropical influences on California precipitation. *J. Climate,* **11,** 412–430.

Molotch, N. P., and R. C. Bales, 2005: Scaling snow observations from the point to the grid element: Implications for observation network design. *Water Resour. Res.,* **41,** W11421, doi:10.1029/2005WR004229.

——, and ——, 2006: SNOTEL representativeness in the Rio Grande headwaters on the basis of physiographics and remotely sensed snow cover persistence. *Hydrol. Processes,* **20,** doi:10.1002/hyp.6128.

National Operational Hydrologic Remote Sensing Center, 2004: Snow Data Assimilation System (SNODAS) data products at NSIDC, November 2003–March 2010. National Snow and Ice Data Center, Boulder, CO, digital media. [Available online at http://nsidc.org/data/docs/noaa/g02158_snodas_snow_cover_model/index.html.]

Neiman, P. J., F. M. Ralph, A. B. White, D. E. Kingsmill, and P. O. G. Persson, 2002: The statistical relationship between upslope flow and rainfall in California's coastal mountains: Observations during CALJET. *Mon. Wea. Rev.,* **130,** 1468–1492.

——, ——, G. A. Wick, Y.-H. Kuo, T.-K. Wee, Z. Ma, G. H. Taylor, and M. D. Dettinger, 2008a: Diagnosis of an intense atmospheric river impacting the Pacific Northwest: Storm summary and offshore vertical structure observed with COSMIC satellite retrievals. *Mon. Wea. Rev.,* **136,** 4398–4420.

——, ——, ——, J. Lundquist, and M. D. Dettinger, 2008b: Meteorological characteristics and overland precipitation impacts of atmospheric rivers affecting the West Coast of North America based on eight years of SSM/I satellite observations. *J. Hydrometeor.,* **9,** 22–47.

——, A. B. White, F. M. Ralph, D. J. Gottas, and S. I. Gutman, 2009: A water vapor flux tool for precipitation forecasting. *Water Manage.,* **162,** 83–94.

Pandey, G. R., D. R. Cayan, and K. P. Georgakakos, 1999: Precipitation structure in the Sierra Nevada of California during winter. *J. Geophys. Res.,* **104,** 12 019–12 030.

Ralph, F. M., P. J. Neiman, and G. A. Wick, 2004: Satellite and CALJET aircraft observations of atmospheric rivers over the eastern North Pacific Ocean during the winter of 1997/98. *Mon. Wea. Rev.,* **132,** 1721–1745.

——, ——, ——, S. I. Gutman, M. D. Dettinger, D. R. Cayan, and A. B. White, 2006: Flooding on California's Russian River: The role of atmospheric rivers. *Geophys. Res. Lett.,* **33,** L13801, doi:10.1029/2006GL026689.

——, ——, G. N. Kiladis, K. Weickmann, and D. W. Reynolds, 2011: A multi-scale observational case study of a Pacific atmospheric river exhibiting tropical–extratropical connections and a mesoscale frontal wave. *Mon. Wea. Rev.,* **139,** 1169–1189.

Tian, B., D. E. Waliser, E. J. Fetzer, and Y. L. Yung, 2010: Vertical moist thermodynamic structure of the Madden–Julian Oscillation in atmospheric infrared sounder retrievals: An update and a comparison to ECMWF Interim Re-Analysis. *Mon. Wea. Rev.,* **138,** 4576–4582.

Uppala, S., D. Dee, S. Kobayashi, P. Berrisford, and A. Simmons, 2008: Towards a climate data assimilation system: Status update of ERA-Interim. *ECMWF Newsletter,* No. 115, ECMWF, Reading, United Kingdom, 52 pp.

Waliser, D. E., 2006: Predictability of tropical intraseasaonal variability. *Predictability of Weather and Climate,* T. Palmer and R. Hagedorn, Eds., Cambridge University Press, 275–305.

Wheeler, M. C., and H. H. Hendon, 2004: An all-season real-time multivariate MJO index: Development of an index for monitoring and prediction. *Mon. Wea. Rev.,* **132,** 1917–1932.

Zhu, Y., and R. E. Newell, 1994: Atmospheric rivers and bombs. *Geophys. Res. Lett.,* **21,** 1999–2002.

——, and ——, 1998: A proposed algorithm for moisture fluxes from atmospheric rivers. *Mon. Wea. Rev.,* **126,** 725–735.